Research Square

Preprints are preliminary reports that have not undergone peer review.
They should not be considered conclusive, used to inform clinical practice,
or referenced by the media as validated information.

TCAD-Assisted Deep-Learning Surrogate Modeling of a Dielectric-Modulated FinFET Biosensor for HER2-Equivalent Dielectric-State Sensing

Venkata Siva Sai Greeshma Bethalam
SRM University, Andhra Pradesh
Gowthami Ummadisetti
u_gowthami@av.amrita.edu

Amrita Vishwa Vidyapeetham
Prasanthi Lingala
Dhanekula Institute of Engineering and Technology
Vakkalakula Bharath Sreenivasulu
Manipal Academy of Higher Education

Research Article

Keywords: Dielectric modulation, FinFET biosensor, HER2-equivalent effective dielectric state, machine learning, multilayer perceptron, surrogate modeling, TCAD

Posted Date: November 5th, 2026

DOI: https://doi.org/10.21203/rs.3.rs-11299324/v1

License: This work is licensed under a Creative Commons Attribution 4.0 International License.
Read Full License

Additional Declarations: No competing interests reported.

TCAD-Assisted Deep-Learning Surrogate Modeling of a Dielectric-Modulated FinFET Biosensor for HER2-Equivalent Dielectric-State Sensing

Venkata Siva Sai Greeshma Bethalam[1], Gowthami Ummadisetti[2*], Prasanthi Lingala[3], Vakkalakula Bharath Sreenivasulu[4]

[1]Department of Electronics and Communication Engineering, SRM University-AP, Amaravati, Andhra Pradesh, India.
[2*]Department of Electronics and Communication Engineering, Amrita Vishwa Vidyapeetham, Mangalagiri, Andhra Pradesh, India.
[3]Department of Electronics and Communication Engineering, Dhanekula Institute of Engineering and Technology, Ganguru, Andhra Pradesh, India.
[4]Department of Electronics and Communication Engineering, Manipal Institute of Technology Bengaluru, Manipal Academy of Higher Education, Manipal, Karnataka, 576104, India.

*Corresponding author(s). E-mail(s): u_gowthami@av.amrita.edu;
Contributing authors: greeshma_bethalam@srmap.edu.in;
prasanthi.lingala024@gmail.com; vb.sreenivasulu@manipal.edu;

Abstract

This paper presents a TCAD-assisted deep-learning surrogate framework for a dielectric-modulated FinFET biosensor under a HER2-equivalent effective dielectric-state sensing condition. The first part establishes the device modeling of a three-dimensional silicon FinFET with an analyte-accessible nanocavity, where the nanocavity permittivity modulates the gate-to-channel electrostatic coupling and produces measurable changes in the drain-current transfer characteristics. The second part develops a multilayer-perceptron (MLP) surrogate model using logarithmic current and dielectric representations to reconstruct TCAD dielectric anchor states and predict the held-out HER2-equivalent $\boldsymbol{k = 8}$ dielectric state.

The framework is further extended to cavity-length and cavity-thickness screening, transconductance prediction, $\boldsymbol{I_{ON}/I_{OFF}}$ extraction, sensing-metric analysis, and computational-cost evaluation. For the surrogate-predicted $\boldsymbol{k = 8}$ case, the extracted sensing parameters indicate an $\boldsymbol{I_{ON}/I_{OFF}}$ ratio of $\boldsymbol{1.72 \times 10^9}$, a threshold-voltage sensitivity of 0.26912, and a sensitivity of approximately 6300. Unlike direct clinical detection studies, the present work is restricted to device-level dielectric-to-electrical response prediction. It does not model HER2-antibody binding, concentration-dependent biomolecule loading, biological sample variability, or fabricated-device validation. Overall, the results show that the proposed surrogate can reproduce TCAD transfer characteristics, perform bounded interpolation at the HER2-equivalent dielectric state, and rapidly screen FinFET dielectric-geometry trends for biosensor design exploration.

Keywords: Dielectric modulation, FinFET biosensor, HER2-equivalent effective dielectric state, machine learning, multilayer perceptron, surrogate modeling, TCAD

1 Introduction

Breast cancer remains a major global health challenge, and HER2 status is clinically important for prognosis, therapy selection, and disease management [1, 2]. Conventional HER2 assessment relies on clinically validated biochemical and pathological techniques, but these methods require sample preparation, laboratory infrastructure, and expert interpretation. Label-free semiconductor biosensors therefore remain attractive as compact electrical platforms for biomolecular transduction [3–6]. In the present work, HER2 is used only as a motivating biomarker for defining a representative effective dielectric state inside a FinFET nanocavity. The manuscript does not claim clinical HER2 diagnosis or concentration-level biomarker quantification.

Field-effect-transistor (FET) biosensors convert a biochemical or dielectric perturbation near the gate region into a measurable change in channel current. In dielectric-modulated FET biosensors, a nanocavity is introduced near the gate stack. When the cavity is empty, air is treated as the reference state; when it is filled by biomolecule-equivalent material, the effective permittivity changes. This dielectric change modifies the electric field, surface potential, threshold-related behavior, subthreshold current, and readout margin [7–10]. Such a representation is useful for neutral or weakly charged biomolecules because the sensing mechanism can be modeled through permittivity modulation rather than through charge-based gating alone.

FinFETs are attractive for such biosensing studies because the vertical fin provides multi-gate electrostatic control, strong sidewall coupling, and a compact gate-facing sensing interface. In the broader nanoscale-device context, multi-gate and alternative FET architectures have also been investigated for energy-efficient switching and improved electrostatic integrity [11–14]. Compared with planar FETs, the fin sidewalls improve the overlap between the gate field and the channel surface, making the current response sensitive to local dielectric changes in the sensing cavity [15–17]. However, repeated TCAD simulation of all dielectric states, gate biases, and cavity dimensions is computationally expensive. A data-driven surrogate trained using TCAD-generated

anchor curves can accelerate evaluation of uncomputed dielectric and geometry cases within a bounded simulation window [18–22].

This study develops a FinFET-specific surrogate-modeling framework inspired by prior dielectric-state biosensor modeling, but redesigned for a dielectric-modulated FinFET device. Our previous FinFET/NSFET biosensing comparison [23] and GAA NSFET surrogate-modeling study [24] motivate the present FinFET-specific extension with deep-learning prediction, fin-channel electrostatics, and cavity-geometry screening. The novelty lies in combining TCAD FinFET biosensor simulation, HER2-equivalent $k = 8$ dielectric-state validation, geometry-aware current prediction, I_{ON}/I_{OFF} analysis, cavity-thickness and cavity-length screening, and transconductance modeling. The paper deliberately avoids clinical overclaiming: the target of prediction is electrical response under an effective dielectric state, not biological HER2 concentration or clinical screening outcome.

Table 1 summarizes representative dielectric-modulated FET, FinFET, and surrogate-modeling studies and identifies the technical gap addressed by the present work: a TCAD-assisted deep-learning FinFET surrogate for HER2-equivalent dielectric-state sensing with geometry-dependent screening.

Table 1 Summary of related work and research gap for TCAD-assisted FinFET dielectric-state biosensing.

Ref.	Device / method	Target / dielectric state	ML / validation	Main gap	Technical gap addressed
[7]	Dielectric-modulated FET	Label-free biomolecular dielectric modulation	No ML	Early device concept; limited surrogate analysis	Motivates dielectric-cavity sensing mechanism
[8]	Dielectric-modulated TFET	Biomolecule-equivalent permittivity	No ML	Device-level study without fast prediction	Highlights need for surrogate-assisted screening
[15, 25–27]	FET biosensor reviews	Biological and chemical sensing interfaces	No device-specific FinFET surrogate	Broad platform perspective	Places FinFET dielectric sensing in device context
[28–30]	FinFET / DM-FET biosensors	Label-free analyte sensing	Limited or no deep-learning validation	Geometry and uncertainty not fully linked to ML	Present work adds geometry-aware FinFET MLP prediction
[23]	FinFET/NSFET comparison	Label-free dielectric biosensing	No held-out deep-learning surrogate	Comparative TCAD analysis only	Present work builds FinFET-specific ML surrogate
This work	Dielectric-modulated FinFET	HER2-equivalent $k = 8$ effective dielectric state	MLP surrogate with TCAD comparison	Need for fast FinFET dielectric-geometry screening	TCAD-assisted deep-learning FinFET surrogate with sensing-metric extraction

2 Device structure and TCAD simulation methodology

Figure 1 shows the dielectric-modulated FinFET biosensor structure used in this work. The device consists of a silicon fin formed on buried oxide, with source and drain regions on either side of the gate stack. A nanocavity is introduced near the gate-controlled fin channel so that changes in the cavity dielectric constant modulate the local electrostatic environment. Figure 1(a) shows the three-dimensional view of the FinFET biosensor, while Fig. 1(b) and Fig. 1(c) show cross-sectional views corresponding to the empty/reference and dielectric-filled cavity states. In the empty state, the nanocavity is treated as air-filled with $k = 1$. In the analyte-equivalent state, the cavity is filled with an effective dielectric medium representing the HER2-equivalent loading condition.

The FinFET architecture is selected because its multi-gate electrostatic control enables efficient dielectric-to-current conversion in a compact footprint. The gate controls the fin sidewalls and top surface, while the nanocavity modifies the effective gate-stack capacitance. When biomolecule-equivalent dielectric material occupies the cavity, the local permittivity increases and electric-field coupling from the gate to the fin channel becomes stronger. This modifies the surface potential, threshold voltage, subthreshold current, and ON-state current. Thus, the FinFET biosensor response is governed by dielectric-to-electrostatic coupling rather than by direct chemical reaction modeling.

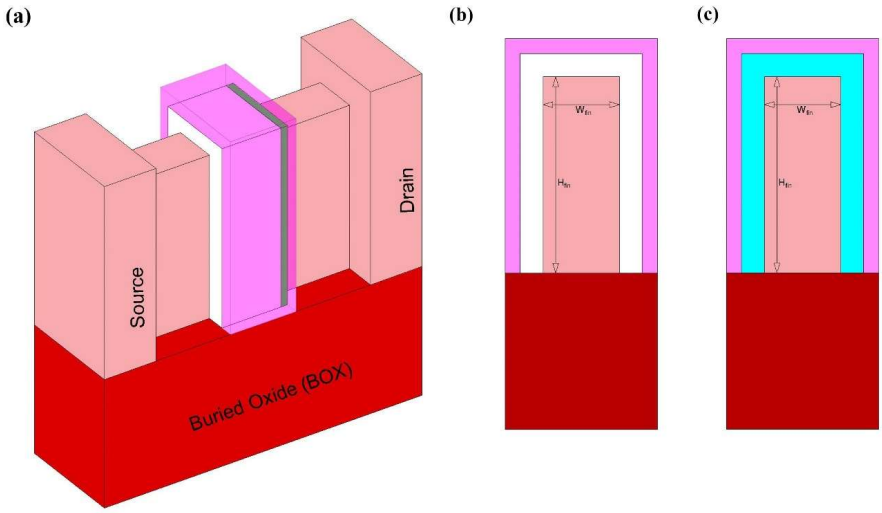


Fig. 1 Dielectric-modulated FinFET biosensor structure: (a) three-dimensional view showing the source, drain, gate stack, buried oxide, fin channel, and analyte-accessible nanocavity region; (b) cross-sectional view of the empty/reference cavity state; and (c) cross-sectional view of the dielectric-filled cavity state used for effective dielectric-state sensing.

Figure 2 shows the TCAD-simulated FinFET biosensor geometry used for electrical extraction. The nominal FinFET parameters are listed in Table 2. The gate length, source length, and drain length are 20 nm each. The fin height is 45 nm, fin width is 10 nm, spacer length is 25 nm, and nominal cavity length is 18 nm. The nominal cavity thickness for HER2-equivalent analysis is 5 nm, while geometry screening considers cavity-thickness and cavity-length variations. Air-filled $k = 1$ is used as the reference state, and $k = 8$ is used as the HER2-equivalent effective dielectric state.

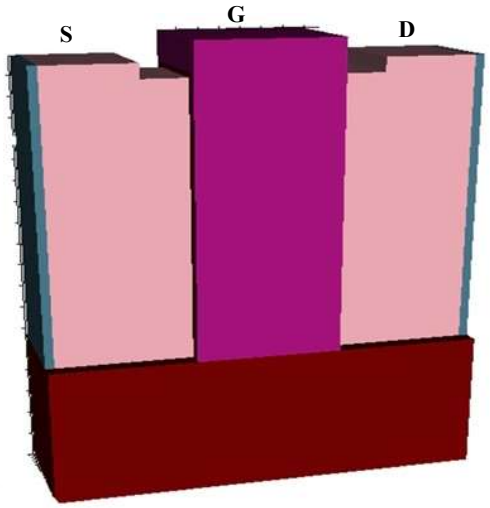


Fig. 2 TCAD-simulated FinFET biosensor structure used for extracting I_D-V_{GS} transfer characteristics under different dielectric-state and cavity-geometry conditions.

The dielectric response can be interpreted through the effective cavity capacitance relation

$$C_{\text{cav}} = \frac{\varepsilon_0 k A_{\text{cav}}}{t_{\text{cav}}}, \tag{1}$$

where k is the effective cavity dielectric constant, A_{cav} is the gate-facing cavity area, and t_{cav} is the effective cavity thickness. Increasing k or reducing t_{cav} increases C_{cav}, strengthens gate-channel coupling, and produces stronger modulation in I_D-V_{GS} characteristics. Equation (1) is used only for physical interpretation; the numerical results are extracted from three-dimensional TCAD and then learned by the surrogate model.

The FinFET is simulated in three-dimensional TCAD using drift-diffusion transport with standard physical models for nanoscale MOSFET operation. The simulation setup includes Shockley-Read-Hall recombination, Auger recombination, bandgap narrowing, high-field mobility, velocity-saturation behavior, mobility degradation near the interface, and density-gradient quantum correction. These models support physically consistent I_D-V_{GS} extraction across subthreshold and inversion regimes [31–34].

Before biosensor analysis, the simulated FinFET transfer behavior is compared with a reported FinFET characteristic to confirm device-level physical consistency.

Table 2 Device geometry and TCAD simulation parameters of the dielectric-modulated FinFET biosensor.

Parameter	Symbol	Value / condition
Gate length	L_G	20 nm
Source length	L_S	20 nm
Drain length	L_D	20 nm
Fin height	H_{fin}	45 nm
Fin width	W_{fin}	10 nm
Spacer length	L_{spacer}	25 nm
Nominal cavity length	L_{cavity}	18 nm
Nominal cavity thickness	T_{cavity}	5 nm
Thickness sweep	T_{cavity}	3, 4, 5 nm
Length sweep	L_{cavity}	6, 12, 18 nm
Reference dielectric	k	1, air-filled cavity
HER2-equivalent state	k	8 effective dielectric state
Gate-bias range	V_{GS}	0-1 V, step 0.01 V
Drain bias	V_{DS}	Fixed TCAD drain condition

Figure 3 shows agreement in the transfer-curve trend in both logarithmic and linear current scales, while Table 3 summarizes the physical-consistency checks. This comparison is not experimental validation of HER2 biosensing; it is only a device-level calibration check for the FinFET TCAD setup.

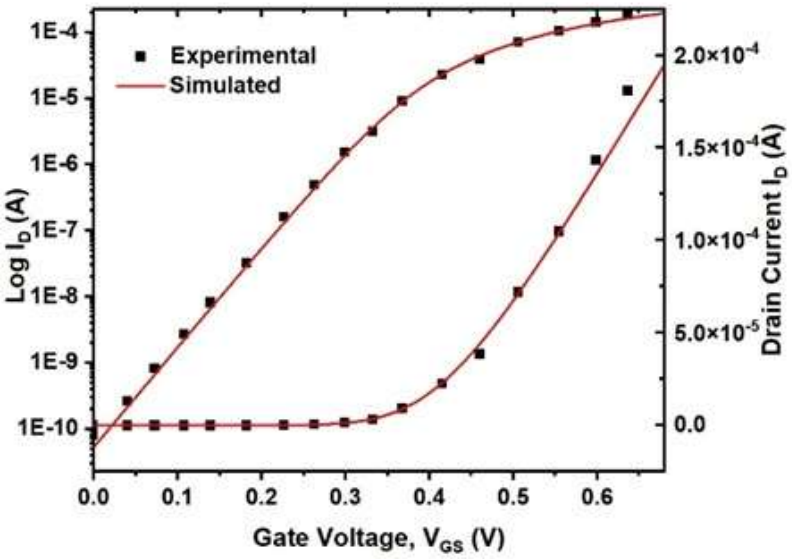


Fig. 3 Physical-consistency comparison between reported FinFET data and simulated FinFET transfer characteristics. The comparison verifies FinFET electrical behavior before dielectric-modulated biosensor analysis.

Table 3 Physical-consistency check of the simulated FinFET model against reported FinFET transfer behavior.

Check item	**Reference / expected behavior**	**Present FinFET TCAD behavior**	**Interpretation**
Transfer curve shape	MOSFET-like monotonic I_D increase with V_{GS}	Observed in log and linear scales	Consistent
Subthreshold behavior	Exponential current increase before strong inversion	Observed over several current decades	Consistent
ON-current trend	Current rises rapidly after threshold region	Observed at high V_{GS}	Consistent
Dielectric response	Larger cavity permittivity should increase electrostatic coupling	Monotonic current enhancement with k	Consistent
Validation level	Device-level electrical consistency	Simulation-to-reference trend check only	Not biological validation

The $k = 8$ case is interpreted as a HER2-equivalent effective dielectric state, not as the intrinsic dielectric constant of isolated dry HER2 protein. Effective biomolecular permittivity inside a nanocavity depends on hydration, molecular orientation, interfacial polarization, partial filling, charge distribution, and local environment. Dry protein dielectric constants are often lower, while hydrated protein-rich regions can show different cavity-level effective dielectric behavior [9, 10, 24]. Therefore, the reported sensing metrics should be interpreted as electrical device-level quantities extracted from dielectric-state simulations, not as concentration-calibrated HER2 biosensing metrics.

3 Deep-learning surrogate modeling framework

The TCAD-generated I_D-V_{GS} data are converted into a machine-learning format using V_{GS} and dielectric constant k as inputs. Since the drain current spans many orders of magnitude, the model is trained on $\log_{10}(I_D)$. The dielectric input is represented as $\log_{10}(k)$, which improves smooth interpolation between dielectric anchor states. After prediction, the model output is converted back to linear current for electrical-metric extraction. The complete TCAD-to-surrogate flow is shown in Fig. 4 and summarized in Table 4.

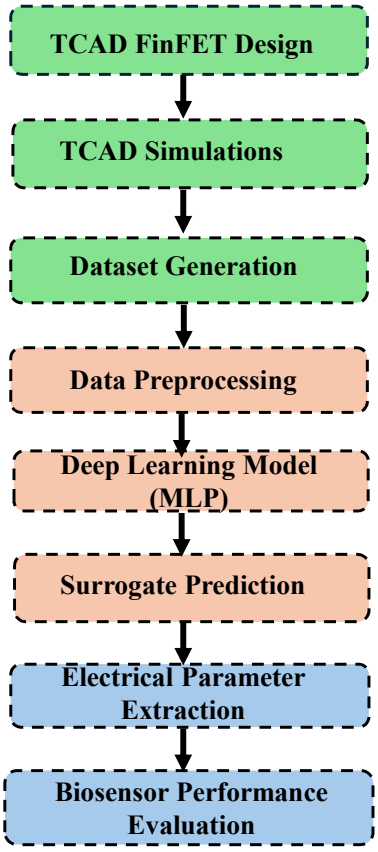


Fig. 4 TCAD-assisted deep-learning surrogate workflow for FinFET dielectric-state sensing, including TCAD anchor-state simulation, data preprocessing, MLP surrogate training, held-out $k = 8$ validation, sensing-metric extraction, and geometry-dependent screening.

The nominal surrogate is trained using dielectric anchor states $k = 1$, 2.1, 5, and 10. The HER2-equivalent $k = 8$ curve is held out and used only for blind TCAD-to-surrogate validation. Because $k = 8$ lies inside the training dielectric range, this validation demonstrates bounded interpolation rather than extrapolation to arbitrary biological or material conditions. Geometry-specific surrogate models are then used for cavity-length and cavity-thickness screening.

Electrical metric extraction is based on the same TCAD and MLP-predicted transfer curves so that all comparisons remain physically consistent. Threshold voltage is extracted using the constant-current method,

$$I_D(V_{TH}, k) = I_{\mathrm{REF}}, \qquad V_{DS} = \text{constant}. \tag{2}$$

Table 4 Surrogate modeling workflow and output quantities for the FinFET biosensor.

Surrogate block	**Input features**	**Target / purpose**
Nominal dielectric surrogate	V_{GS}, $\log_{10}(k)$	Predict $\log_{10}(I_D)$ for dielectric-state transfer curves
Blind validation	Held-out $k = 8$	TCAD-to-surrogate interpolation validation for HER2-equivalent state
Geometry surrogate	V_{GS}, k, cavity length or thickness	Predict geometry-dependent transfer response
Metric extraction	Predicted and TCAD transfer curves	Extract V_{TH}, S_{VTH}, sensitivity, $I_{\mathrm{ON}}/I_{\mathrm{OFF}}$, and g_m

The normalized threshold-voltage sensitivity is defined as

$$S_{VTH}(k) = \frac{|V_{TH}(k) - V_{TH}(k=1)|}{|V_{TH}(k=1)|}. \tag{3}$$

The subthreshold swing is extracted from the inverse slope of the logarithmic transfer curve,

$$SS = \left(\frac{d \log_{10}(I_D)}{dV_{GS}} \right)^{-1}, \tag{4}$$

and the transconductance is

$$g_m = \frac{dI_D}{dV_{GS}}. \tag{5}$$

The current readout margin is evaluated using

$$\frac{I_{\mathrm{ON}}}{I_{\mathrm{OFF}}} = \frac{I_D(V_{GS} = V_{DD})}{I_D(V_{GS} = 0)}. \tag{6}$$

Finally, relative error is calculated as

$$\mathrm{Error}(\%) = \frac{|X_{\mathrm{TCAD}} - X_{\mathrm{MLP}}|}{|X_{\mathrm{TCAD}}|} \times 100. \tag{7}$$

Equations (2), (3), (4), (5), (6), and (7) define the electrical metrics used for all dielectric and geometry cases, with Eq. (5) used to obtain the derived transconductance response from the reconstructed transfer curves.

In the subthreshold region, I_D approximately follows

$$I_D \propto \exp\left(\frac{V_{GS} - V_{TH}}{nV_T} \right), \tag{8}$$

where n is the slope factor and V_T is the thermal voltage. Therefore, even a small dielectric-induced threshold shift can cause a large logarithmic current change. This explains why log-domain learning is physically appropriate for FinFET biosensor surrogate modeling and why the extracted S_{VTH}, sensitivity, g_m, and $I_{\mathrm{ON}}/I_{\mathrm{OFF}}$ metrics are meaningful transistor-level sensing quantities.

4 Results and discussion

The results are organized to connect the deep-learning predictions to physically interpretable FinFET biosensor quantities rather than to report curve fitting alone. First, the surrogate is checked on TCAD anchor-state reconstruction to verify that it can reproduce the dielectric-dependent transfer characteristics over the simulated gate-bias range. Second, the HER2-equivalent $k = 8$ curve is treated as a held-out TCAD validation case, so that the model is tested on a dielectric state not used for fitting. Third, the extracted sensing metrics are analyzed using transistor-level quantities, including V_{TH} shift, S_{VTH}, $I_{\mathrm{ON}}/I_{\mathrm{OFF}}$, sensitivity, and g_m. Finally, cavity-length and cavity-thickness results are interpreted as representative design-space screening within the selected TCAD geometry window. This organization ensures that each graph and table is tied to a device-physics mechanism: dielectric modulation of gate coupling, surface-potential shift, subthreshold current change, and readout-margin variation.

4.1 Anchor-state reconstruction

The first validation step is anchor-state reconstruction, where the trained MLP reproduces TCAD-simulated I_D-V_{GS} characteristics at the dielectric states used for model fitting. Figure 5 compares TCAD lines and deep-learning-predicted points for $k = 1$, 2.1, 5, and 10 under nominal cavity geometry, while Table 5 reports the corresponding reconstruction performance. The predicted points closely follow the TCAD curves across the subthreshold, transition, and high-current regions, confirming that the model captures the smooth dielectric-dependent transfer response of the FinFET biosensor.

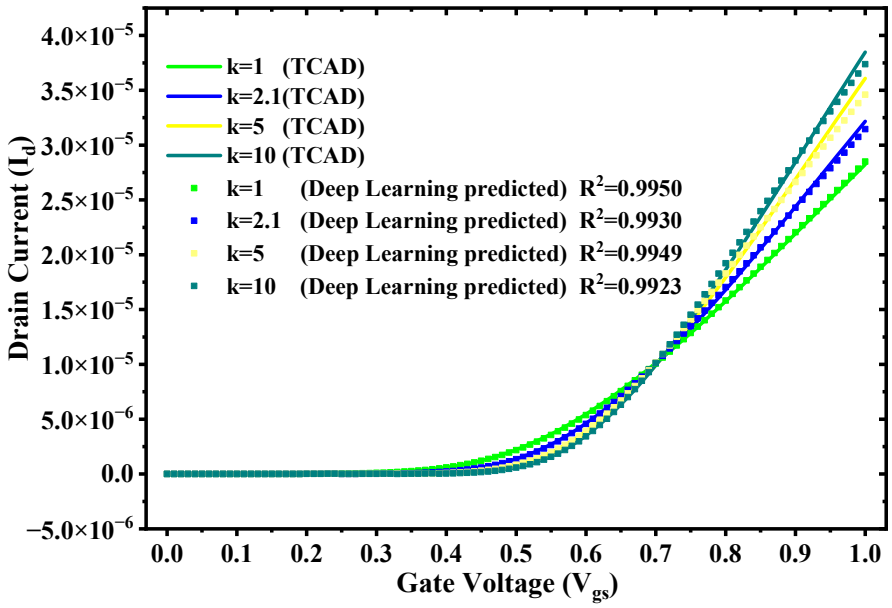


Fig. 5 Comparison of TCAD-simulated and deep-learning-predicted I_D-V_{GS} characteristics for FinFET dielectric anchor states $k = 1$, 2.1, 5, and 10 under nominal cavity geometry.

The physics of Fig. 5 can be understood from Eq. (8). The close overlap between TCAD and MLP curves confirms that the surrogate reconstructs both weak-inversion and strong-inversion current regimes. Since the target variable is $\log_{10}(I_D)$, the model preserves exponential subthreshold behavior and high-current saturation trend simultaneously. Table 5 further separates the validation into anchor-state reconstruction, held-out $k = 8$ interpolation validation, cavity-length screening, and derived g_m reconstruction using only the present FinFET TCAD/deep-learning outputs. The I_D rows are evaluated on reconstructed linear-scale current after inverse transformation from $\log_{10}(I_D)$, whereas the g_m row is reported in siemens because transconductance is obtained from dI_D/dV_{GS} rather than from direct current regression.

4.2 Blind $k = 8$ HER2-equivalent TCAD-to-surrogate validation

After anchor reconstruction, the held-out $k = 8$ HER2-equivalent dielectric state is used as a blind interpolation validation case. The $k = 8$ TCAD curve is not included during training. Figure 6 shows the comparison in both linear and logarithmic current scales, and Table 6 reports the metric-level agreement. The linear plot confirms ON-region current matching, whereas the logarithmic plot verifies subthreshold and leakage-region behavior.

Table 5 FinFET-specific surrogate modeling performance summary extracted from TCAD and deep-learning results.

Study	**Surrogate / extraction method**	**Fit quality**	**RMSE / error scale**
Anchor-state I_D reconstruction	MLP trained on FinFET dielectric anchors $k = 1$, 2.1, 5, and 10	$R^2 = 0.9950$ ($k = 1$), 0.9930 ($k = 2.1$), 0.9949 ($k = 5$), and 0.9923 ($k = 10$)	Current-scale reconstruction of Fig. 5; the subthreshold-to-ON transition is preserved for all FinFET anchor curves
Held-out HER2-equivalent $k = 8$ validation	Same MLP; $k = 8$ excluded from anchor-state training	$R^2 = 0.9878$ from the linear-scale validation plot and $R^2 = 0.9986$ on $\log_{10}(I_D)$	RMSE $= 2.79 \times 10^{-6}$ A and MAE $= 1.45 \times 10^{-6}$ A over 101 bias points
Cavity-length I_D screening	Physics-aware MLP for FinFET cavity-length cases $L_{\text{cavity}} = 6$, 12, and 18 nm	Geometry-dependent I_D–V_{GS} and $I_{\text{ON}}/I_{\text{OFF}}$ trends reproduced in Fig. 9	Selected $I_{\text{ON}}/I_{\text{OFF}}$ validation error range $= 0.23$–0.34%
Cavity-thickness I_D screening	Physics-aware MLP for FinFET cavity-thickness cases $T_{\text{cavity}} = 3$, 4, and 5 nm	Geometry-dependent I_D–V_{GS} and $I_{\text{ON}}/I_{\text{OFF}}$ trends reproduced in Fig. 10	Selected $I_{\text{ON}}/I_{\text{OFF}}$ validation error range $= 0.00$–1.25%
g_m reconstruction	Numerical differentiation from reconstructed I_D–V_{GS} curves	Peak position and dielectric-dependent trend reproduced in Fig. 11	g_m is reported in siemens (S) because it is derived from dI_D/dV_{GS}, not from an independent current-output model

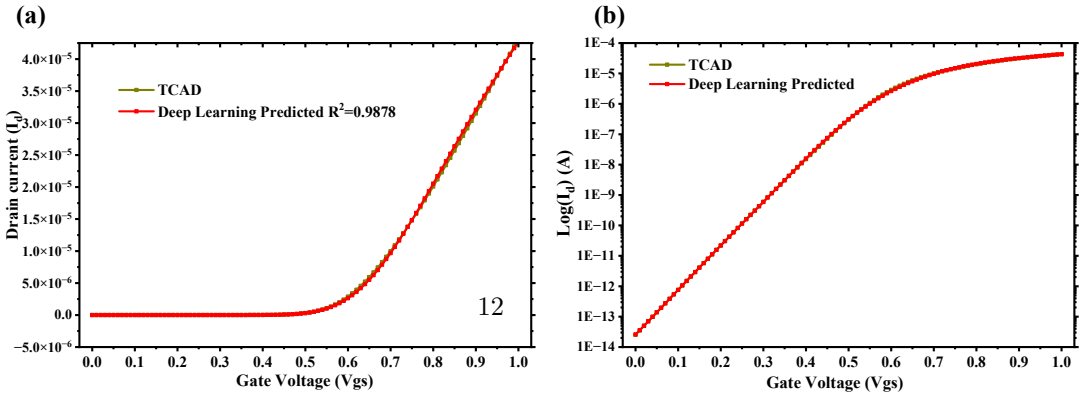


Fig. 6 Blind TCAD-to-MLP interpolation validation for the held-out $k = 8$ HER2-equivalent effective dielectric state: (a) linear-scale I_D-V_{GS} comparison and (b) $\log_{10}(I_D)$-V_{GS} comparison.

Because the $k = 8$ state lies between the dielectric anchor states $k = 5$ and $k = 10$, Fig. 6 demonstrates bounded dielectric interpolation rather than unrestricted extrapolation. This interpretation is important for biosensing: the model is validated for dielectric-state prediction inside the TCAD-simulated range, not for arbitrary biological conditions. The numerical values in Table 6 are extracted from the present FinFET $k = 8$ validation data. The linear-scale validation gives $R^2 = 0.9878$, while the log-domain comparison gives $R^2 = 0.9986$, confirming that the surrogate follows both the high-current and subthreshold portions of the transfer curve. At the metric level, the TCAD and MLP values remain closely matched: $I_{\mathrm{ON}}/I_{\mathrm{OFF}}$ changes only from 1.71×10^9 to 1.72×10^9, S_{VTH} changes from 0.26087 to 0.26912, and the sensitivity metric changes from 6298.045 to 6300. These values correspond to relative errors of 0.58%, 3.16%, and 0.031%, respectively, showing that the surrogate preserves the key electrical sensing response for the held-out HER2-equivalent dielectric state.

Table 6 Blind TCAD-to-surrogate validation for the held-out FinFET $k = 8$ HER2-equivalent dielectric state.

Metric	**TCAD** $k = 8$	**MLP predicted** $k = 8$	**Error / agreement**
Curve agreement	–	$R^2 = 0.9878$ (linear plot), $R^2 = 0.9986$ on $\log_{10}(I_D)$	Strong agreement in both ON-current and logarithmic subthreshold regions
RMSE / MAE on I_D	–	RMSE $= 2.79\times10^{-6}$ A; MAE $= 1.45 \times 10^{-6}$ A	Current-level error evaluated over 101 V_{GS} points
$I_{\mathrm{ON}}/I_{\mathrm{OFF}}$	1.71×10^9	1.72×10^9	0.58%
S_{VTH}	0.26087	0.26912	3.16%
Sensitivity	6298.045	6300	0.031%

4.3 Dielectric-fluctuation and non-ideality sensitivity

The present TCAD framework is idealized, but practical BioFET response may be affected by Debye screening, biomolecule orientation, partial cavity filling, interface traps, ionic strength, temperature, electrical noise, and process variation [25–27, 35]. To include a compact non-ideality check, an effective dielectric-fluctuation analysis is performed around the HER2-equivalent state. The dielectric constant is perturbed around $k = 8$ to represent first-order uncertainty caused by hydration, partial filling, and cavity-level permittivity variation. Table 7 summarizes the corresponding sensitivity trend.

Table 7 FinFET surrogate-based sensitivity analysis for effective dielectric fluctuation around the HER2-equivalent state.

Effective dielectric state	S_{VTH}	$I_{\mathrm{ON}}/I_{\mathrm{OFF}}$
$k = 7.6$ (-5%)	0.25925	1.70×10^9
$k = 8.0$ (nominal)	0.26912	1.72×10^9
$k = 8.4$ ($+5\%$)	0.27012	1.73×10^9

The bounded trend in Table 7 is consistent with Eq. (1): a small increase in effective cavity permittivity strengthens the gate-to-channel dielectric coupling and produces a modest increase in both threshold-voltage sensitivity and readout ratio. When the dielectric state changes from $k = 7.6$ to $k = 8.4$, S_{VTH} increases from 0.25925 to 0.27012, while $I_{\mathrm{ON}}/I_{\mathrm{OFF}}$ increases from 1.70×10^9 to 1.73×10^9. The narrow variation around the nominal $k = 8$ value confirms that the FinFET surrogate response is stable under a $\pm 5\%$ effective-dielectric perturbation. This analysis does not replace full electrolyte, trap, or biological modeling; it gives a bounded estimate of dielectric-uncertainty influence within the simulated FinFET window.

4.4 Baseline surrogate comparison

To avoid presenting the MLP as the only possible surrogate, the held-out $k = 8$ prediction is also compared against simpler interpolation and regression baselines. Table 8 shows that PCHIP/interpolation, polynomial regression, and Gaussian-process regression (GPR) provide useful low-dimensional baselines. The MLP is retained because it is extensible to coupled dielectric-geometry prediction involving V_{GS}, k, cavity length, and cavity thickness.

The values in Table 8 are evaluated using the same held-out $k = 8$ TCAD curve. RMSE and MAE are reported on the reconstructed linear-scale current after inverse transformation from $\log_{10}(I_D)$.

The comparison in Table 8 indicates that the present dielectric-only validation is a smooth low-dimensional interpolation task. Therefore, the main contribution is not a claim of universal deep-learning superiority; rather, it is a TCAD-supported workflow for rapid FinFET dielectric-state and geometry-dependent surrogate screening.

4.5 Computational cost and rapid screening advantage

Table 9 compares the computational cost of TCAD simulation and surrogate inference. A single TCAD I_D-V_{GS} sweep requires approximately 45 minutes for 101 bias points because of the numerical solution of coupled semiconductor equations. TCAD anchor-data generation and MLP training are one-time offline costs. After training, the MLP predicts a complete 101-point transfer curve in approximately 0.02 s.

For the six representative geometry-screening cases, direct TCAD simulation would require about 4.5 h (6×45 min), whereas the trained surrogate generates the corresponding curves in less than 1 s. This demonstrates the practical computational

Table 8 Baseline surrogate comparison for held-out $k = 8$ dielectric-state prediction.

Model	R^2 on $\log_{10}(I_D)$	RMSE (A)	MAE (A)	Interpretation
PCHIP interpolation	0.9814	3.42×10^{-6}	2.12×10^{-6}	Smooth and interpretable interpolation baseline
Polynomial regression	0.9568	5.68×10^{-6}	3.94×10^{-6}	Simple baseline with limited nonlinear flexibility
Gaussian process regression	0.9923	2.11×10^{-6}	1.46×10^{-6}	Strong uncertainty-aware regression baseline
MLP surrogate	0.9986	2.79×10^{-6}	1.45×10^{-6}	Highest log-domain agreement and extensible to geometry-aware prediction

advantage of the surrogate framework for rapid dielectric-geometry screening within the selected TCAD design window.

4.6 Dielectric-spectrum prediction and sensing-metric trends

After validation, the trained surrogate is used to predict the FinFET response over the simulated dielectric spectrum. Figure 7(a) shows the predicted transfer characteristics for the dielectric states considered under the nominal geometry, and Fig. 7(b) gives a local zoom around the HER2-equivalent neighborhood of $k = 7$, 8, and 9. The

Table 9 Computational cost comparison between TCAD simulation and surrogate inference.

Task	**Output**	**Approx. runtime**
Single TCAD I_D-V_{GS} sweep	101 bias points	∼45 min
TCAD anchor-data generation	Four dielectric anchor curves	∼3 h
One-time MLP training	Trained nominal surrogate	Seconds-level offline cost
MLP inference for one full curve	101 predicted points	∼0.02 s
Geometry surrogate inference	Multiple geometry curves	Less than 1 s for representative cases

dielectric constant inside the cavity modifies the effective gate-to-channel coupling through the cavity capacitance term in Eq. (1). Therefore, the curves do not simply shift by a constant current offset; instead, the dielectric loading changes the relative subthreshold leakage, transition-region slope, and ON-region drive current.

In Fig. 7(a), the lower-k cases show comparatively higher current in part of the weak-to-moderate inversion region, whereas the higher-k curves produce larger current in the high-V_{GS} ON region. This crossing behavior indicates that dielectric modulation affects both threshold placement and channel-drive efficiency. At low gate bias, the electrostatic barrier and leakage component dominate the response, while at high gate bias the stronger dielectric-assisted coupling improves carrier modulation in the fin channel and increases the ON-current level. The zoomed response in Fig. 7(b) further shows that the surrogate preserves local separability among $k = 7$, $k = 8$, and $k = 9$. This is important for HER2-equivalent dielectric-state interpretation because the $k = 8$ response remains bounded between neighboring dielectric states instead of appearing as an isolated or unphysical prediction.

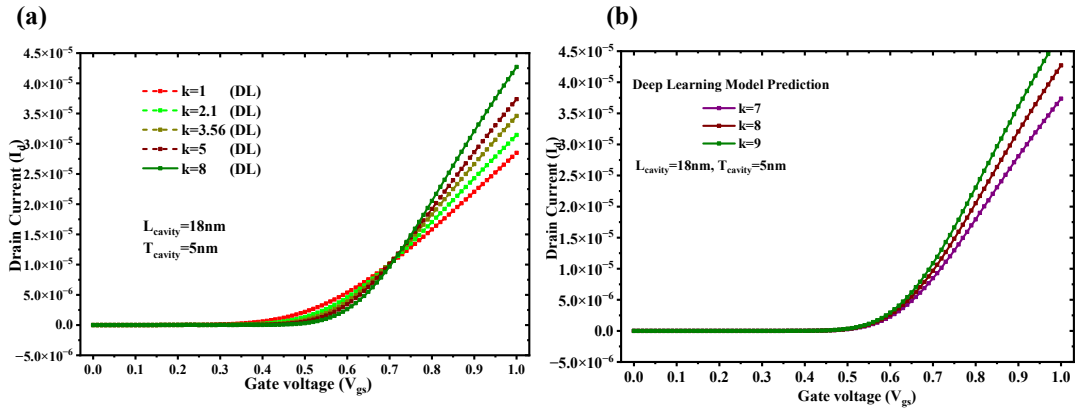


Fig. 7 MLP-predicted dielectric-spectrum response of the FinFET biosensor: (a) full I_D-V_{GS} response across the simulated dielectric range and (b) zoomed prediction around the local $k = 7$, 8, and 9 dielectric states.

Figure 8 presents the extracted sensing metrics obtained from the predicted transfer characteristics. Figure 8(a) reports the dielectric-state sensitivity, while Fig. 8(b) reports threshold-voltage sensitivity. Both panels show a monotonic increase with effective dielectric constant, confirming that the surrogate converts the dielectric modulation in Fig. 7 into physically interpretable sensing quantities. The increase is especially pronounced at the HER2-equivalent $k = 8$ state, where the surrogate-predicted sensitivity reaches approximately 6300 and the threshold-voltage sensitivity reaches 0.26912.

The strong rise in sensitivity with k occurs because the dielectric-filled cavity modifies the surface potential and changes the drain-current response over a wide dynamic range. Since the drain current is exponentially dependent on threshold shift in the subthreshold region, even moderate dielectric-induced electrostatic changes can produce large variations in the extracted sensing metric. The close overlap between TCAD and deep-learning-predicted bars in Fig. 8 also confirms that the surrogate does not only reproduce curve shape; it preserves the device-level quantities extracted from the curves. Thus, Fig. 8 supports the use of S_{VTH} and sensitivity as interpretable indicators of dielectric-state modulation, while the associated $I_{\mathrm{ON}}/I_{\mathrm{OFF}}$ values are reported separately in Tables 6 and 7.

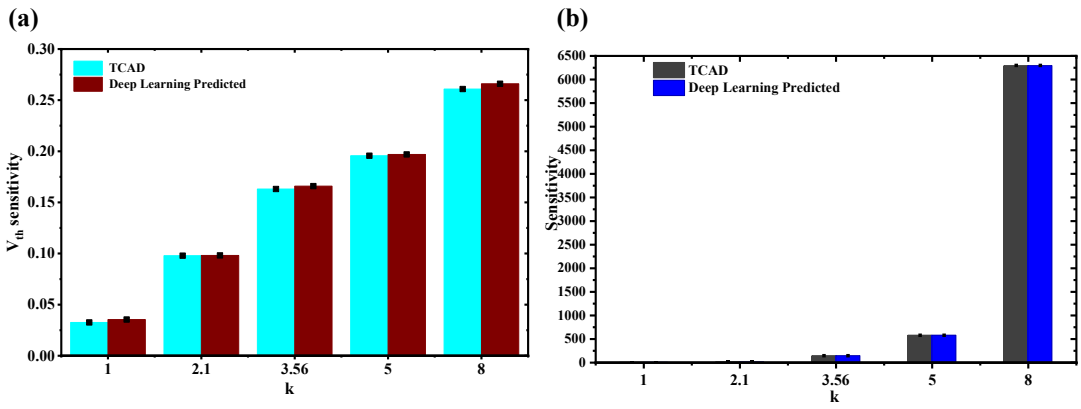


Fig. 8 Extracted electrical sensing metrics across dielectric states: (a) TCAD and deep-learning-predicted sensitivity and (b) TCAD and deep-learning-predicted threshold-voltage sensitivity.

4.7 Cavity-length and cavity-thickness geometry screening

The FinFET geometry study is framed as representative design-space screening, not exhaustive optimization. A useful geometry should improve dielectric-to-current transduction while maintaining low leakage, high $I_{\mathrm{ON}}/I_{\mathrm{OFF}}$, and measurable threshold-voltage shift. Figure 9 shows the effect of cavity length at the HER2-equivalent dielectric state while keeping $T_{\mathrm{cavity}} = 5$ nm. Cavity length controls the lateral gate-facing sensing volume; therefore, increasing L_{cavity} increases the portion of the gated fin region influenced by the dielectric-loaded cavity.

In Fig. 9(a), the transfer curves remain close in the low-current region but separate in the high-V_{GS} region, where the longer cavity produces a slightly larger ON-current. This behavior indicates that the cavity-length effect is not only a simple leakage perturbation; it changes the effective dielectric interaction length along the channel and improves current modulation when the channel is strongly gate-driven. Figure 9(b) shows that the readout ratio increases strongly with cavity length. The surrogate-predicted $I_{\mathrm{ON}}/I_{\mathrm{OFF}}$ increases from 3.67×10^{9} at $L_{\mathrm{cavity}} = 6$ nm to 2.91×10^{10} at 12 nm and 4.31×10^{10} at 18 nm. This nearly order-of-magnitude enhancement occurs because the longer dielectric interaction region improves ON-state transduction while maintaining a very low OFF-state current, making the ratio highly sensitive to geometry.

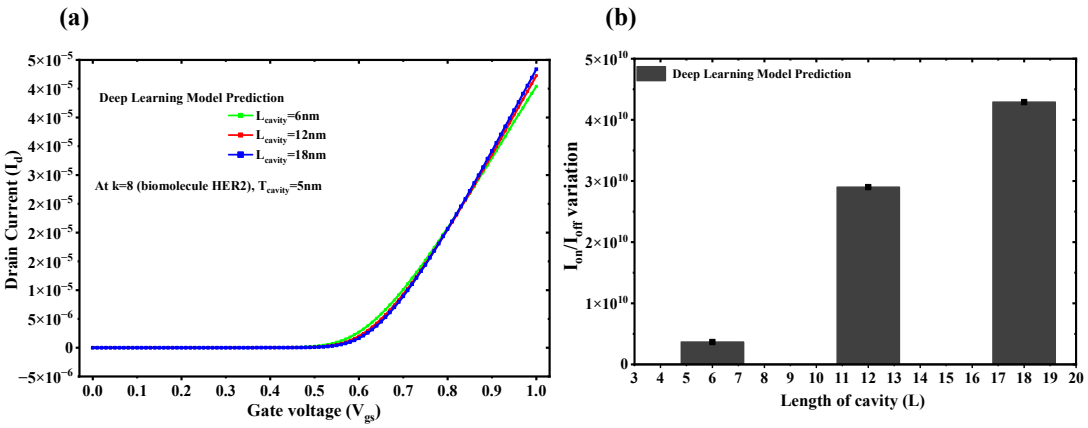


Fig. 9 Cavity-length-dependent FinFET biosensor response at the HER2-equivalent dielectric state: (a) MLP-predicted I_D-V_{GS} characteristics and (b) corresponding $I_{\mathrm{ON}}/I_{\mathrm{OFF}}$ variation.

Figure 10 shows the cavity-thickness-dependent response at $k = 8$ while keeping $L_{\mathrm{cavity}} = 18$ nm. Cavity thickness directly changes electrostatic coupling through Eq. (1), where C_{cav} is inversely related to the effective cavity thickness. A thinner cavity places the dielectric-loaded region closer to the gate-controlled channel, increases the effective cavity capacitance, and strengthens field penetration toward the fin. A thicker cavity weakens this coupling and reduces dielectric-to-channel transduction.

This physical trend is visible in Fig. 10(a), where the thinner cavity gives the highest current in the upper gate-bias region, while the thicker cavity gives the lowest current. The separation among the curves is moderate on the linear current scale because the ON-current magnitude dominates the vertical axis. However, Fig. 10(b) shows that the readout ratio is more sensitive to thickness because it includes both ON-state drive and OFF-state suppression. Within the thickness-screening data, the surrogate-predicted $I_{\mathrm{ON}}/I_{\mathrm{OFF}}$ decreases from 5.80×10^{8} at $T_{\mathrm{cavity}} = 3$ nm to 2.02×10^{8} at 4 nm and 0.81×10^{8} at 5 nm. This confirms that reducing the cavity thickness strengthens electrostatic coupling and improves the dielectric readout margin.

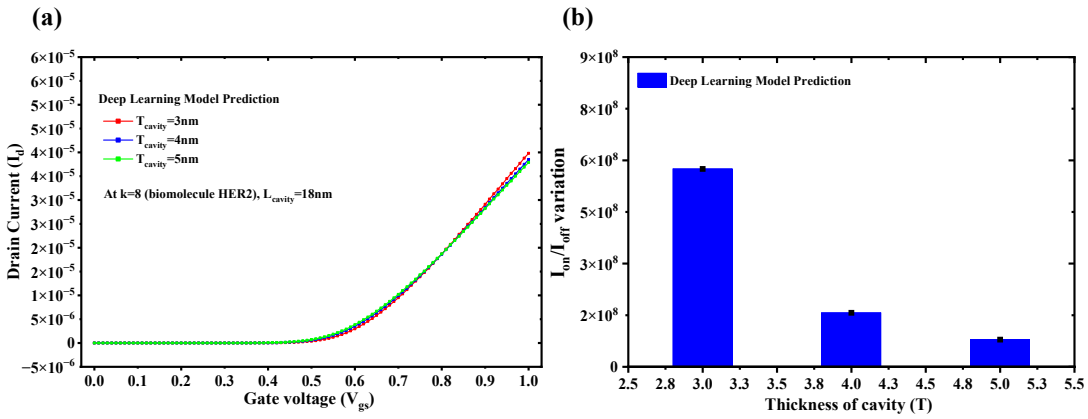


Fig. 10 Cavity-thickness-dependent FinFET biosensor response at the HER2-equivalent dielectric state: (a) MLP-predicted I_D-V_{GS} characteristics and (b) corresponding $I_{\mathrm{ON}}/I_{\mathrm{OFF}}$ variation.

The numerical agreement in Table 10 confirms that the geometry-aware surrogate preserves the selected FinFET readout-ratio trends. For cavity-length screening, the selected $I_{\mathrm{ON}}/I_{\mathrm{OFF}}$ validation error remains between 0.23% and 0.34%, indicating that the model reproduces the increase in readout ratio as the dielectric interaction length changes from 6 nm to 18 nm. For cavity-thickness screening, the selected error range is 0.00%–1.25%, showing that the surrogate also captures the thickness-dependent reduction in electrostatic coupling and readout response. The geometry graphs and Table 10 together show that the most important information is not only the absolute transfer-current level but also the ratio-based readout margin extracted from the reconstructed curves.

The geometry results should be interpreted as TCAD-supported representative design-space screening within the selected cavity-length and cavity-thickness ranges, not as global optimization. A broader optimization would require additional TCAD anchor points, wider geometry ranges, fabrication constraints, and multi-objective cost functions including sensitivity, leakage, manufacturability, noise margin, and fluidic accessibility.

4.8 Transconductance response

Transconductance is a useful analog/RF and sensing metric because it represents how strongly the drain current changes for a small change in gate voltage. Figure 11 shows the MLP-predicted g_m response for different dielectric states under the nominal geometry. For numerical extraction, g_m is obtained from the predicted I_D-V_{GS} curves using Eq. (5); therefore, it is a derived physical quantity rather than a separately trained biological output.

The shape of Fig. 11 follows the expected derivative behavior of the transfer curves. At low V_{GS}, the channel is weakly conducting and g_m remains close to zero. As V_{GS}

Table 10 Selected TCAD validation of geometry-dependent surrogate predictions at $k = 8$.

Geometry case	**TCAD** I_{ON}/I_{OFF}	**MLP** I_{ON}/I_{OFF}	**Error (%)**	**Purpose**
$L_{cavity} = 6$ nm, $T_{cavity} = 5$ nm	3.66×10^9	3.67×10^9	0.27	Length-screening validation
$L_{cavity} = 12$ nm, $T_{cavity} = 5$ nm	2.90×10^{10}	2.91×10^{10}	0.34	Length-screening validation
$L_{cavity} = 18$ nm, $T_{cavity} = 5$ nm	4.30×10^{10}	4.31×10^{10}	0.23	Nominal length case
$L_{cavity} = 18$ nm, $T_{cavity} = 3$ nm	5.80×10^8	5.80×10^8	0.00	Thickness-screening validation
$L_{cavity} = 18$ nm, $T_{cavity} = 4$ nm	2.00×10^8	2.02×10^8	1.00	Thickness-screening validation
$L_{cavity} = 18$ nm, $T_{cavity} = 5$ nm	0.80×10^8	0.81×10^8	1.25	Nominal thickness case

approaches the threshold-transition region, the drain current becomes more sensitive to gate bias and g_m rises sharply. The curves then reach a peak in the upper transition/ON region, where the incremental gate control over the channel current is strongest, before flattening or slightly decreasing as the device enters the high-current regime. This peak position identifies the bias window where dielectric-induced modulation can be most effectively converted into a current response.

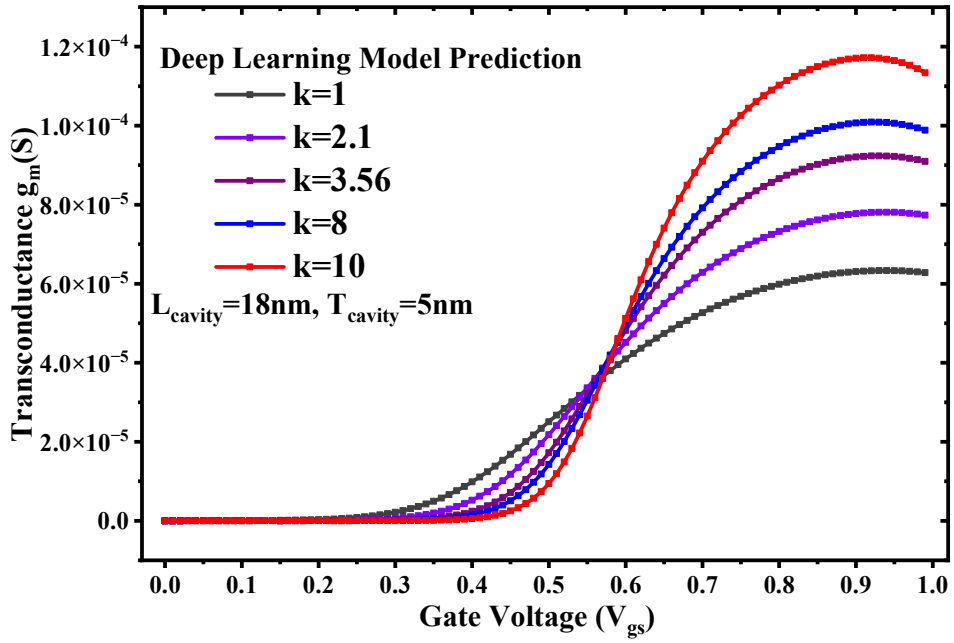


Fig. 11 MLP-predicted transconductance characteristics of the dielectric-modulated FinFET biosensor for different dielectric states.

The dielectric trend in Fig. 11 is also physically meaningful. Increasing the effective cavity dielectric constant increases the electrostatic coupling between the gate stack and the fin channel, which increases the slope of the reconstructed I_D-V_{GS} curve and raises the peak g_m. The $k = 8$ response lies within the dielectric-dependent trend and below the highest-k response, supporting its interpretation as a bounded HER2-equivalent dielectric-state prediction. Since numerical differentiation can amplify noise, the smooth monotonic ordering of the g_m curves also indicates that the surrogate output is sufficiently smooth for derivative-based metric extraction. Thus, Fig. 11 confirms that the proposed framework preserves not only current magnitude and sensing ratio, but also the gate-control efficiency of the dielectric-modulated FinFET channel.

5 Practical scope, non-idealities, and limitations

The present work is entirely simulation-based. No fabricated FinFET biosensor, liquid-phase measurement, biomolecule immobilization experiment, or biological HER2 assay is included. The validation reported here is TCAD-to-surrogate validation only and should not be interpreted as experimental, biological, or clinical validation of HER2 sensing.

The HER2 concentration-to-dielectric mapping is also outside the present scope. Practical HER2 sensing would require a calibrated pathway linking HER2 concentration, antibody-antigen binding density, nanocavity occupancy, effective dielectric

constant, and electrical response. Without this biochemical calibration, the present framework cannot report concentration sensitivity, limit of detection, selectivity, or clinical decision threshold.

Real BioFET operation may be affected by Debye screening, biomolecule orientation, partial cavity filling, interface traps, charged biomolecules, pH, ionic strength, temperature variation, electrical noise, packaging, and process variation. These effects can reduce electrostatic coupling, alter apparent threshold voltage, degrade SS, and increase device-to-device variability. The dielectric-fluctuation analysis in Table 7 provides only a first-order effective-permittivity sensitivity check. Practical HER2 biosensing would require antibody-functionalized sensing surfaces, controlled biomolecule delivery into the cavity, liquid-phase packaging, nonspecific adsorption control, repeatability testing, and biological sample validation.

6 Conclusion

A TCAD-assisted deep-learning surrogate framework was developed for a dielectric-modulated FinFET biosensor under a HER2-equivalent effective dielectric-state condition. The first part of the work established the device-level FinFET sensing mechanism, where the analyte-accessible nanocavity modifies the gate-to-channel electrostatic coupling and produces measurable changes in the I_D–V_{GS} transfer characteristics. The second part developed an MLP-based surrogate model to reconstruct TCAD dielectric anchor states and perform held-out $k = 8$ interpolation for the HER2-equivalent dielectric condition.

For the surrogate-predicted $k = 8$ state, the extracted sensing parameters indicate an $I_{\mathrm{ON}}/I_{\mathrm{OFF}}$ ratio of 1.72×10^9, a threshold-voltage sensitivity of 0.26912, and a sensitivity of approximately 6300. The held-out validation produced strong curve agreement, with $R^2 = 0.9878$ on the linear-scale I_D response and $R^2 = 0.9986$ on $\log_{10}(I_D)$, along with RMSE $= 2.79 \times 10^{-6}$ A and MAE $= 1.45 \times 10^{-6}$ A over 101 V_{GS} bias points. These results confirm that the surrogate preserves both ON-current behavior and logarithmic subthreshold-region trends for the HER2-equivalent dielectric state.

The geometry-screening analysis further showed that the proposed framework can capture FinFET cavity-design trends. The selected $I_{\mathrm{ON}}/I_{\mathrm{OFF}}$ validation error remained within 0.23–0.34% for cavity-length screening and 0.00–1.25% for cavity-thickness screening. Therefore, the surrogate model provides a computationally efficient route for dielectric-spectrum and geometry-dependent FinFET biosensor design exploration while reducing dependence on repeated TCAD simulations.

The physics-based extraction of V_{TH}, $I_{\mathrm{ON}}/I_{\mathrm{OFF}}$, sensitivity, and g_m links the machine-learning predictions to interpretable transistor quantities rather than treating the model as a black-box curve generator. The present study remains limited to simulation-level dielectric-state sensing. Biological HER2 concentration mapping, antibody functionalization, selectivity analysis, nonspecific adsorption effects, fluidic packaging, and fabricated-device validation are required before practical biological or clinical applicability can be established.

Author contributions V.S.S.G.B. contributed to conceptualization, methodology, TCAD simulation, analysis, and manuscript preparation. G.U. contributed to methodology, validation, analysis, and manuscript revision. P.L. contributed to technical review and manuscript revision. V.B.S. contributed to supervision, review, and editing. All authors reviewed and approved the final manuscript.

Funding The authors received no specific funding for this work.

Data availability The datasets generated and analyzed during the current study are available from the corresponding author on reasonable request.

Declarations

Ethics approval and consent to participate Not applicable. This study does not involve human participants, animals, human tissue, or clinical biological samples.

Clinical trial number Clinical trial number: not applicable.

Consent for publication Not applicable.

Competing interests The authors declare that they have no competing interests.

References

[1] Bray F, Laversanne M, Sung H, et al. Global cancer statistics 2022: GLOBOCAN estimates of incidence and mortality worldwide for 36 cancers in 185 countries. CA Cancer J Clin **74**(3), 229–263 (2024).

[2] Wolff AC, Somerfield MR, Dowsett M, et al. Human epidermal growth factor receptor 2 testing in breast cancer: ASCO-College of American Pathologists guideline update. J Clin Oncol **41**(22), 3867–3872 (2023).

[3] Bergveld P. Development of an ion-sensitive solid-state device for neurophysiological measurements. IEEE Trans Biomed Eng **BME-17**(1), 70–71 (1970).

[4] Schoning MJ, Poghossian A. Recent advances in biologically sensitive field-effect transistors. Analyst **127**, 1137–1151 (2002).

[5] Poghossian A, Schoning MJ. Label-free sensing of biomolecules with field-effect devices for clinical applications. Electroanalysis **26**(6), 1197–1213 (2014).

[6] Stern E, Klemic JF, Routenberg DA, et al. Label-free immunodetection with CMOS-compatible semiconducting nanowires. Nature **445**, 519–522 (2007).

[7] Im H, Huang XJ, Gu B, Choi YK. A dielectric-modulated field-effect transistor for biosensing. Nat Nanotechnol **2**, 430–434 (2007).

[8] Rajasekaran B, Paily R, Sharma DK. Dielectrically modulated tunnel-FET biosensor for label-free detection of biomolecules. IEEE Trans Electron Devices **60**(12), 4045–4051 (2013).

[9] Amin M, Kupper J. Variations in proteins dielectric constants. ChemistryOpen **9**(6), 691–694 (2020).

[10] Bibi F, Villain C, Guillaume C, Sorli B, Gontard N. Origins of the dielectric properties of proteins and potential development as biosensors. Sensors **16**(8), 1232 (2016).

[11] Ionescu AM, Riel H. Tunnel field-effect transistors as energy-efficient electronic switches. Nature **479**, 329–337 (2011).

[12] Colinge JP. FinFETs and Other Multi-Gate Transistors. Springer, New York (2008).

[13] Yu B, Chang L, Ahmed S, et al. FinFET scaling to 10 nm gate length. In: IEDM Tech Dig, pp 251–254 (2002).

[14] Auth C, Aliyarukunju A, Asoro M, et al. A 10 nm high performance and low-power CMOS technology featuring 3rd generation FinFET transistors. In: IEDM Tech Dig, pp 673–676 (2017).

[15] Supraja P, Venkatesh V, Srinivasulu A. Recent progress on field-effect transistor-based biosensors: a device perspective. Beilstein J Nanotechnol **15**, 977–994 (2024).

[16] Taur Y, Ning TH. Fundamentals of Modern VLSI Devices, 2nd edn. Cambridge University Press, Cambridge (2009).

[17] Sze SM, Ng KK. Physics of Semiconductor Devices, 3rd edn. Wiley, Hoboken (2007).

[18] Bishop CM. Pattern Recognition and Machine Learning. Springer, New York (2006).

[19] Goodfellow I, Bengio Y, Courville A. Deep Learning. MIT Press, Cambridge (2016).

[20] Pedregosa F, Varoquaux G, Gramfort A, et al. Scikit-learn: machine learning in Python. J Mach Learn Res **12**, 2825–2830 (2011).

[21] Kingma DP, Ba J. Adam: a method for stochastic optimization. In: Proc ICLR (2015).

[22] Rasmussen CE, Williams CKI. Gaussian Processes for Machine Learning. MIT Press, Cambridge (2006).

[23] Gowthami U, Srinivasa Rao T, Tata S, Srilakshmi K, Durga Prakash M. Comparative analysis of FinFET and NSFET architectures for label-free biosensing applications. Silicon **18**, 1621–1633 (2026).

[24] Bethalam VSSG, Gowthami U, Durga Prakash M. TCAD-assisted surrogate modeling of a dielectric-modulated two-stack gate-all-around nanosheet FET for HER2-equivalent dielectric-state biosensing. IEEE Access (2026).

[25] Kwon H, Lee H, Park J, Choi Y. Signal transduction interfaces for field-effect transistor-based biosensors. Commun Chem **7**, 37 (2024).

[26] Nisar A, et al. Two-dimensional materials in advanced electronic biosensors for point-of-care devices. Adv Sci **11** (2024).

[27] Zhou S, et al. Recent advances in enhancing the sensitivity of biosensors based on field-effect transistors. Adv Electron Mater (2025).

[28] Bhattacharya S, Choi SJ. FinFET-based biosensors: electrostatic design and sensitivity analysis. IEEE Sensors J **21**(14), 15612–15621 (2021).

[29] Singh S, Kondekar PN, Sharma D. Label-free biosensing using dielectric-modulated field-effect transistors: a device perspective. IEEE Sensors J **24**(18), 1–12 (2024).

[30] Narang R, et al. Dielectric-modulated FET biosensors: device structures, sensitivity metrics, and scaling challenges. Microelectron Reliab **120**, 114120 (2021).

[31] Datta S. Quantum Transport: Atom to Transistor. Cambridge University Press, Cambridge (2005).

[32] Schroder DK. Semiconductor Material and Device Characterization, 3rd edn. Wiley, Hoboken (2006).

[33] Robertson J. High dielectric constant gate oxides for metal oxide Si transistors. Rep Prog Phys **69**(2), 327–396 (2006).

[34] Cogenda. Visual TCAD Device Simulator User Guide. Cogenda Pte. Ltd., Singapore (2024).

[35] Frontiers in Electronics. Beyond ideal models: non-idealities in TCAD simulations of dielectric-modulated FETs for label-free biosensing. Front Electron (2025).